






Elucidating biophysical basis of binding of inhibitors to SARS-CoV-2 main protease by using molecular dynamics simulations and free energy calculations

Md Fulbabu Sk , Rajarshi Roy , Nisha Amarnath Jonniya, Sayan Poddar and Parimal Kar 

Discipline of Biosciences and Biomedical Engineering, Indian Institute of Technology Indore, Indore, MP, India

Communicated by Ramaswamy H. Sarma

ABSTRACT

The recent outbreak of novel “coronavirus disease 2019” (COVID-19) has spread rapidly worldwide, causing a global pandemic. In the present work, we have elucidated the mechanism of binding of two inhibitors, namely α -ketoamide and Z31792168, to SARS-CoV-2 main protease (M^{pro} or $3CL^{pro}$) by using all-atom molecular dynamics simulations and free energy calculations. We calculated the total binding free energy (ΔG_{bind}) of both inhibitors and further decomposed ΔG_{bind} into various forces governing the complex formation using the Molecular Mechanics/Poisson-Boltzmann Surface Area (MM/PBSA) method. Our calculations reveal that α -ketoamide is more potent ($\Delta G_{bind} = -9.05$ kcal/mol) compared to Z31792168 ($\Delta G_{bind} = -3.25$ kcal/mol) against COVID-19 $3CL^{pro}$. The increase in ΔG_{bind} for α -ketoamide relative to Z31792168 arises due to an increase in the favorable electrostatic and van der Waals interactions between the inhibitor and $3CL^{pro}$. Further, we have identified important residues controlling the $3CL^{pro}$ -ligand binding from per-residue based decomposition of the binding free energy. Finally, we have compared ΔG_{bind} of these two inhibitors with the anti-HIV retroviral drugs, such as lopinavir and darunavir. It is observed that α -ketoamide is more potent compared to lopinavir and darunavir. In the case of lopinavir, a decrease in van der Waals interactions is responsible for the lower binding affinity compared to α -ketoamide. On the other hand, in the case of darunavir, a decrease in the favorable intermolecular electrostatic and van der Waals interactions contributes to lower affinity compared to α -ketoamide. Our study might help in designing rational anti-coronaviral drugs targeting the SARS-CoV-2 main protease.

Abbreviation: AM1-BCC: Austin Model 1- Bond Charge Correction; $3CL^{pro}$: Chymotrypsin-like protease; COVID-19: Coronavirus Disease 2019; DCC: Dynamic Cross Correlation; dPCA: Dihedral Principal Component Analysis; DRV: Darunavir; GAFF: Generalized Amber Force Field; HIV: Human Immunodeficiency Virus; LPV: Lopinavir; MD: Molecular Dynamics; MMPBSA: Molecular Mechanics Poisson-Boltzmann Surface Area; nCoV: Novel Coronavirus; NMA: Normal Mode Analysis; PCA: Principal Component Analysis; PME: Particle-Mesh Ewald; RMSD: Root Mean Square Deviations; RMSF: Root Mean Square Fluctuations; SARS-CoV-2: Severe Acute Respiratory Syndrome-Coronavirus-2; SASA: Solvent Accessible Surface Area; TIP3P: Transferable Inter-Potential with 3 Point Charge

ARTICLE HISTORY

Received 12 April 2020

Accepted 7 May 2020

KEYWORDS

COVID-19; SARS-CoV-2
 $3CL^{pro}$; Molecular
Dynamics; MM-PBSA;
binding free energy

1. Introduction

The recent outbreak of “coronavirus disease 2019” (COVID-19) poses a severe public health risk. COVID-19 is caused by the novel coronavirus (nCoV) or SARS-CoV-2, which is a highly contagious and pathogenic virus (Aanouz et al., 2020; Pant et al., 2020). The disease has spread worldwide since its outbreak in the city of Wuhan, China, in 2019 (Boopathi et al., 2020; Hasan et al., 2020; Hui et al., 2020; Sinha et al., 2020; Wu et al., 2020). So far, the total number of people diagnosed with the COVID-19 viral infection exceeds over 3.7 million, with more than 0.26 million fatalities worldwide. In India, more than 50000 people have been infected, including 1700 deaths (<https://www.mohfw.gov.in>). The number of positive cases is increasing exponentially due to human-to-human transmission. The World Health Organisation (WHO)

has declared COVID-19 a global pandemic. nCoV is a non-segmented, single-stranded, positive-sense RNA virus that belongs to the beta coronavirus family (Woo et al., 2010; Elmezayen et al., 2020; Enayatkhani et al., 2020; Gupta et al., 2020). This gene encodes four structural proteins, namely spike glycoprotein (S), a small envelope protein (E), matrix glycoprotein (M), and nucleocapsid protein (N) (Rota et al., 2003; Elfiky 2020; Elfiky 2020; Elfiky & Azzam, 2020). The S protein attaches with the host receptor by the specific receptor binding domain (RBD) (Wan et al., 2020), while the N protein binds to RNA in multiple sites to make a helical nucleocapsid structure (Chang et al., 2014; Jin et al., 2020). Along with these proteins, chymotrypsin-like cysteine protease ($3CL^{pro}$) is an essential protein for maintaining the viral life cycle by cleaving the essential polyprotein PP1A to individual functional components. $3CL^{pro}$ contains 9 α -helices

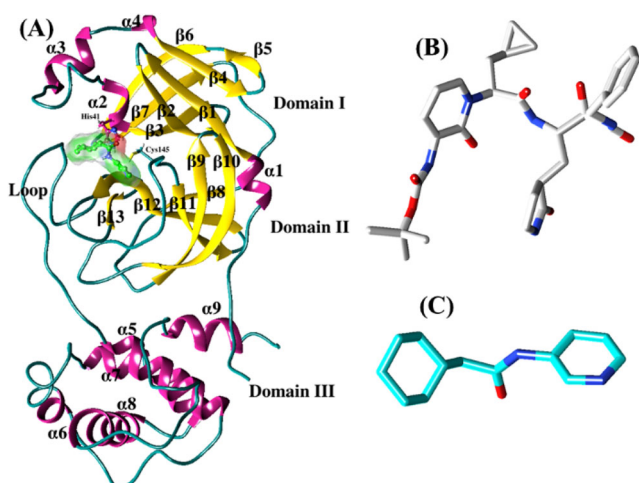


Figure 1. (A) The ribbon representation of SARS-CoV-2 3CL^{PRO}. The catalytic dyad residues (H41 and C145) are shown in balls and sticks. The inhibitors, α -ketoamide (B) and Z31792168 (C) are represented as sticks.

and 13 β -strands (see Figure 1(A)), creating three domains, domain I (residues 8-101), domain II (residues 102-184), and domain III (residues 201-306). The domains II and III are connected by a long loop (residues 185-200). The active site of this protease is located between domains I and II, and each domain contributes a single residue to the catalytic dyad, His41 and Cys145, respectively. 3CL^{PRO} plays a crucial role in mediating viral replication and transcription making it an attractive drug target for the treatment of COVID-19.

Recently, Jin and co-workers have designed a modified peptide inhibitor for this protease and solved the X-ray crystal structure of the complex (Jin et al., 2020). The availability of the crystal structure of 3CL^{PRO} opens up a lot of opportunities to develop new antiviral drugs. This structure is employed to computationally evaluate the repurposing of different FDA approved drugs against COVID-19 (Das, Sarmah, Lyndem & Singha Roy 2020; Islam et al., 2020; Joshi et al., 2020; Wang, 2020). Several studies have predicted the binding strength of darunavir, indinavir, like other HIV protease drugs and some other small molecules against 3CL^{PRO} (Alamri et al., 2020; Abdelli et al., 2020; Khan et al., 2020; Khan et al., 2020; Lin et al., 2020; Muralidharan et al., 2020; Sang et al., 2020; Sarma et al., 2020; Umesh et al., 2020; Wahedi et al., 2020).

Recently, Zhang and co-workers have designed a potent inhibitor, α -ketoamide [tert-butyl (1-((S)-1-(((S)-4-(benzylamino)-3,4-dioxo-1-((S)-2-oxopyrrolidin-3-yl)butan-2-yl)amino)-3-cyclopropyl-1-oxopropan-2-yl)-2-oxo-1,2-dihydropyridin-3-yl)carbamate] (see Figure 1(B)) targeting 3CL^{PRO} and resolved the crystal structure of 3CL^{PRO}/ α -ketoamide (Zhang et al., 2020). This inhibitor shows a promising binding as well as a pronounced lung tropism and can be administered by the inhalation route (Zhang et al., 2020). In the present work, we have studied the mechanism of binding of this inhibitor to SARS-CoV-2 3CL^{PRO} using molecular dynamics simulations in conjunction with the popular molecular mechanics/Poisson-Boltzmann surface area scheme. We have also considered another inhibitor, Z31792168 (2-cyclohexyl-N-pyridin-3-yl-ethanamide) (Fearon et al., 2020) in our study (see Figure 1(C)) and compared with α -ketoamide. Finally, the binding free energy

of these two inhibitors is compared with the anti-HIV retroviral drugs, such as lopinavir and darunavir.

2. Materials and methods

2.1. Simulation protocol

The initial coordinates for our molecular dynamics simulations were obtained from the X-ray crystallographic structure of the SARS-CoV-2 3CL^{PRO} complexed with the inhibitors α -ketoamide (PDB: 6Y2G) and Z31792168 (PDB: 5R84) (Berman et al., 2002; Zhang et al., 2020). The missing residues in 3CL^{PRO} were added by using the Modeller (Fiser & Šali, 2003; Webb & Sali, 2014) plugin in UCSF Chimera software (Pettersen et al., 2004). The protonation states of the charged residues were determined using the Propka 3.1 webserver (Olsson et al., 2011). All simulations were executed by the *pmemd.cuda* module of AMBER18 (Case et al., 2018) package and analyses were done by the Cpptraj module (Roe & Cheatham, 2013). We used the latest AMBER ff14SB force field (Maier et al., 2015) to describe the protein structure and the updated generalized Amber force field (GAFF2) (Wang et al., 2004) is used to assign parameters to small molecules. All the missing hydrogen atoms were added by the *Leap* module of AMBER (Salomon-Ferrer et al., 2013). The inhibitors were assigned AM1-BCC (Jakalian et al., 2002) charge, which was calculated by utilizing the Antechamber (Wang et al., 2006) module of AMBER18. The systems were solvated in a truncated octahedron periodic box with an explicit TIP3P (Price & Brooks, 2004) water model and a 10 Å buffer distance was considered from the complex along each side.

A suitable integer number of counterions (Na^+) were added for neutralizing the whole system. The temperature was kept at 300 K and controlled by the Langevin thermostat (Loncharich et al., 1992). The system pressure was monitored using a Berendsen Barostat (Berendsen et al., 1984) and kept at 1.0 bar. All bond lengths involving hydrogen atoms were constrained by the SHAKE algorithm (Kräutler et al., 2001). We used a time-step of 2.0 fs for the simulation. The particle mesh Ewald summation (PME) (Darden et al., 1993) approach was used to compute the long-range electrostatic interactions. For all cases, the nonbonded cut-off was fixed at 10.0 Å.

Firstly, each complex was optimized using 500 steps of the steepest descent algorithm followed by another 500 cycles of the conjugate gradient scheme. During the minimization, the receptor-inhibitor complexes were restrained to their respective coordinates with a force constant of 2.0 kcal $\text{mol}^{-1}\text{\AA}^{-2}$. Next, we carried out the minimization without applying any harmonic restraint on the solutes to remove any residual steric clashes. After the minimization, the temperature of each solvated system was gradually increased from 0 K to 300 K at the NVT (canonical) ensemble with a restraint force constant of 2.0 kcal $\text{mol}^{-1}\text{\AA}^{-2}$ acting on the solute atoms. Subsequently, a 50 ps MD simulation with a restraint force constant of 2.0 kcal $\text{mol}^{-1}\text{\AA}^{-2}$ acting on all solute atoms at a constant pressure of 1.0 atm was conducted using Berendsen Barostat (Berendsen et al., 1984) at a fixed

temperature of 300 K. After 1.0 ns of an equilibration phase, the production simulation was carried for 100 ns at the NPT ensemble. The Cartesian coordinates were stored every 10 ps. Overall, we accumulated 10000 snapshots corresponding to each production simulation.

2.2. Dynamic cross-correlation map (DCCM)

The correlated and non-correlated atomic motions of complex protein residues were computed with the help of DCCM (McCammon, 1984; Hünenberger et al., 1995) analysis using Cpptraj (Roe & Cheatham, 2013) module of AmberTools19. Herein, we avoid the apparent correlations between slow side-chain fluctuations and backbone movements. To reduce the statistical noise, we considered only C_{α} atomic coordinates of each residue. The cross-correlations between the residues were described by the covariance matrix, and the element C_{ij} of the covariance matrix was calculated using the following equation:

$$C_{ij} = \frac{\langle \Delta r_i * \Delta r_j \rangle}{(\sqrt{\langle \Delta r_i^2 \rangle} * \sqrt{\langle \Delta r_j^2 \rangle})} \quad (1)$$

where Δr_i and Δr_j represent the displacements from the average position of i^{th} and j^{th} atoms with respect to time, respectively. The angular bracket indicates the time average over the entire trajectory. The cross-correlated values vary between -1 and 1. The positive value represents the positively correlated motions, while negative values represent the anti-correlated motions. We have considered the final 90 ns production simulation trajectories for this analysis.

2.3. Principal component analysis (PCA)

PCA or principal component analysis (Ichiye & Karplus, 1991) gives us detailed information about residual movements and functional significance of each residue. Similar to DCCM analysis, only C_{α} atomic coordinates were used for this analysis. The atomic fluctuations of C_{α} -atoms of each residue form a covariance matrix, as described in the DCC analysis. The diagonalization of the covariance matrix gives us the orthogonal eigenvectors and the corresponding eigenvalues. The eigenvectors indicate the directions of the concerted motions, and the eigenvalues describe the amplitude of the motions. These eigenvectors and associate eigenvalues represent the set of principal components (PCs), which may be used to describe the movement characteristics. We also calculated the cosine content via GROMACS (g_covar, g_anaeig, and g_analyze modules) (Hess et al., 2008) of first few PCs to check the statistical convergence significance of each trajectory. The higher value of conformational sampling convergence gives a low value of cosine contents. Our first few PC's cosine contents values lie between 0 to 0.6 for each case, which indicates a high conformational sampling convergence.

2.4. Free energy landscape

The free energy landscape (FEL) calculations were performed by AmberTools19 Cpptraj module of AMBER18 using the below Equation (2) (Frauenfelder et al., 1991);

$$G_i = -k_B T \ln \left(\frac{N_i}{N_m} \right) \quad (2)$$

where k_B represents the Boltzmann constant, T is the temperature of each simulated system. N_i is the population of the i^{th} bin, and N_m is the population of the most populated bin. Therefore, bins with no population are an artificial barrier as an indication of the lowest probability. To measure the conformational variability of each system in terms of FELs, we considered the first two principal components (PC1 and PC2) as reaction coordinates.

2.5. Energy calculations

In order to estimate the stabilization of binding systems, the binding free energies or affinity of all inhibitors against SARS-CoV-2 3CL^{PRO} were calculated by the widely used molecular mechanics Poisson-Boltzmann surface area (MM-PBSA) method (Kollman et al., 2000; Wang et al., 2001; Kar et al., 2007; Kar et al., 2007; Kar et al., 2011; Kar & Knecht, 2012a; Kar & Knecht, 2012b; Kar & Knecht, 2012c; Kar & Knecht, 2012d; Kar et al., 2013). We discussed the MMPBSA scheme in detail in our previous studies (Jonniya et al., 2019; Jonniya & Kar, 2020; Roy et al., 2020; Sk et al., 2020) and here we used the same protocol. Briefly, in the MMPBSA scheme, the binding free energy (ΔG_{bind}) of an inhibitor is calculated by utilizing the following equations:

$$\Delta G_{bind} = \Delta H - T\Delta S \approx \Delta E_{MM} + \Delta G_{solv} - T\Delta S \quad (3)$$

$$\Delta E_{MM} = \Delta E_{internal} + \Delta E_{elec} + \Delta E_{vdW} \quad (4)$$

$$\Delta G_{solv} = \Delta G_{pol} + \Delta G_{np} \quad (5)$$

Where ΔE_{MM} , ΔG_{solv} and $-T\Delta S$ are the changes in molecular mechanics (MM) energy at the gas phase, desolvation free energy and the conformational entropy upon complexation, respectively. Further, ΔE_{MM} is sum of $\Delta E_{internal}$ (bond, dihedral and angle energies), ΔE_{elec} (electrostatic), and ΔE_{vdW} (van der Waals) energies while ΔG_{solv} includes ΔG_{pol} (polar solvation energy) and ΔG_{np} (nonpolar solvation energy). The normal mode analysis (Xu et al., 2011) method was used to calculate the configurational entropy (S_{MM}). Due to the high computational cost, we considered only 50 configurations from the last 20 ns simulations for entropy calculations. We were also performed the per-residue decomposition of binding energy by molecular mechanics generalize- Born surface area (MM-GBSA) scheme to know the individual residual contributions of each residue. All the parameters used in this calculation were developed by Onufriev and Bashford (Onufriev et al., 2004). In this study, 2000 structural frames were applied to run the MM-PBSA calculation.

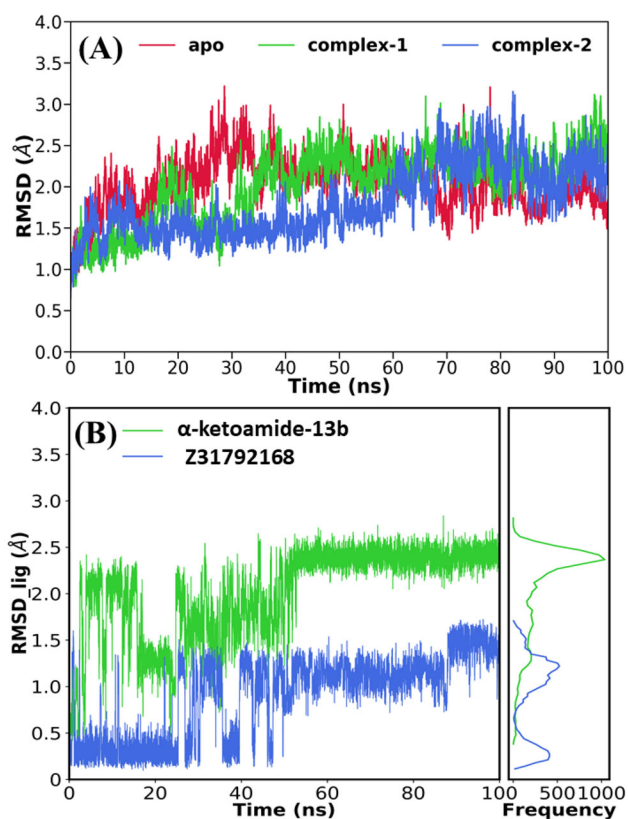


Figure 2. Time evolution of root-mean-square deviations (RMSD) of (A) backbone atoms of 3CL^{Pro} relative to their respective minimized structure and (B) heavy atoms of inhibitor.

2.6. Hydrogen bond criterion

The hydrogen bonds between the inhibitor and receptor were analyzed using the Cpptraj module in AmberTools19 (Roe & Cheatham, 2013). The formation of hydrogen bond defined by a distance and an angle cut-off of ≤ 3.5 Å and $\geq 120^\circ$, respectively, between the donor (D) and acceptor (A) atom.

3. Results and discussion

3.1. Structural stability and flexibility analysis

To verify the convergence of our simulations, we estimated the root-mean-square deviations (RMSDs) of backbone atoms relative to the initial structure, and the temporal RMSD of all systems is shown in Figure 2. From Figure 2(A), it is clear that apo 3CL^{Pro} reached a stable equilibrium after 30 ns while the 3CL^{Pro}/α-ketoamide system reached equilibrium after 40 ns. In the case of 3CL^{Pro}/Z31792168, the equilibrium is reached after 60 ns.

The average RMSDs for all simulated systems were calculated and reported in Table 1. The average RMSD was found to vary between 1.95 Å and 2.25 Å for all cases. The highest deviation (2.25 Å) was obtained for 3CL^{Pro}/α-ketoamide, while the lowest RMSD (1.95 Å) was obtained for 3CL^{Pro}/Z31792168. We also calculated the RMSD of each ligand, and the time evolution of ligand RMSD is shown in Figure 2(B). As can be seen from Figure 2(B), two inhibitors reached equilibrium after 50 ns of MD simulations. In the case of α-ketoamide, the frequency distribution of RMSD is characterized by a sharp peak at 2.4 Å

Table 1. The average RMSD, solvent accessible surface area (SASA), and radius of gyration for the simulated systems.

System	Backbone RMSD (Å)	SASA (Å ²)	Radius of gyration (R _g) (Å)
apo	2.10 (0.01)	14650 (3.5)	22.13 (0.01)
3CL ^{Pro} /α-ketoamide	2.25 (0.01)	13969 (3.2)	22.03 (0.01)
3CL ^{Pro} /Z31792168	1.95 (0.01)	14208 (3.6)	21.96 (0.01)

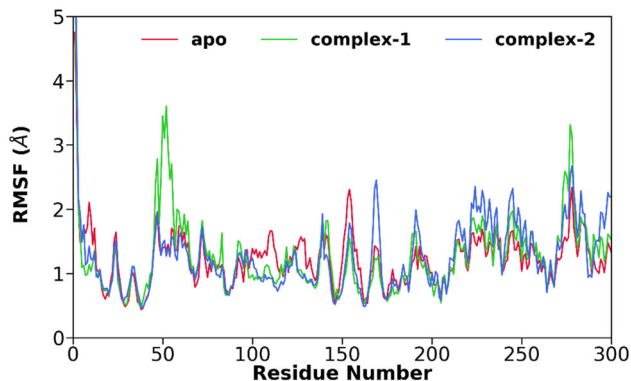


Figure 3. The root-mean-square fluctuations (RMSFs) of C_α atoms for apo (red), 3CL^{Pro}/α-ketoamide (green), and 3CL^{Pro}/Z31792168 (blue).

while two peaks (0.23 Å and 1.1 Å) are obtained for Z31792168. The K-mean cluster analysis of the ligand suggests two dominant conformations for both ligands, and these conformations correspond to dominant poses in the binding cavity (see Supporting Information Figure S1).

Next, we investigated the flexibility of different parts of 3CL^{Pro} by calculating the root mean square fluctuations (RMSFs) of C_α-atoms for all systems and is shown in Figure 3. It is evident from Figure 3 that all three systems display more or less similar fluctuations. In the case of apo-3CL^{Pro}, domain II (residues 102-184) shows slightly higher fluctuations, which gets diminished after the ligand binding. In the case of 3CL^{Pro}/α-ketoamide, a relatively higher value of RMSF is obtained around residue 50 (domain I) compared to apo or 3CL^{Pro}/Z31792168.

The structural compactness of each system was analyzed by estimating the radius of gyration (R_g) from their respective MD trajectories, and the calculated average values are reported in Table 1. A similar R_g is obtained for all systems. Finally, the solvent-accessible surface area (SASA) that indicates the degree of solvent exposure was also calculated and reported in Table 1. It is evident from Table 1 that SASA values vary between 13969 Å² and 14650 Å² for all systems. The highest value (14650 Å²) was obtained for apo, while the lowest SASA value (13969 Å²) was reported for 3CL^{Pro}/α-ketoamide. An intermediate SASA value (14208 Å²) was obtained for 3CL^{Pro}/Z31792168.

3.2. Dynamic cross-correlation (DCC) analysis

To elucidate the effect of inhibitor-binding on the internal dynamics of 3CL^{Pro}, the cross-correlation matrix was calculated by using the coordinates of C_α atoms from MD trajectories, and the dynamic cross-correlation map (DCCM) is displayed in Figure 4. Overall, after the inhibitor binding, a

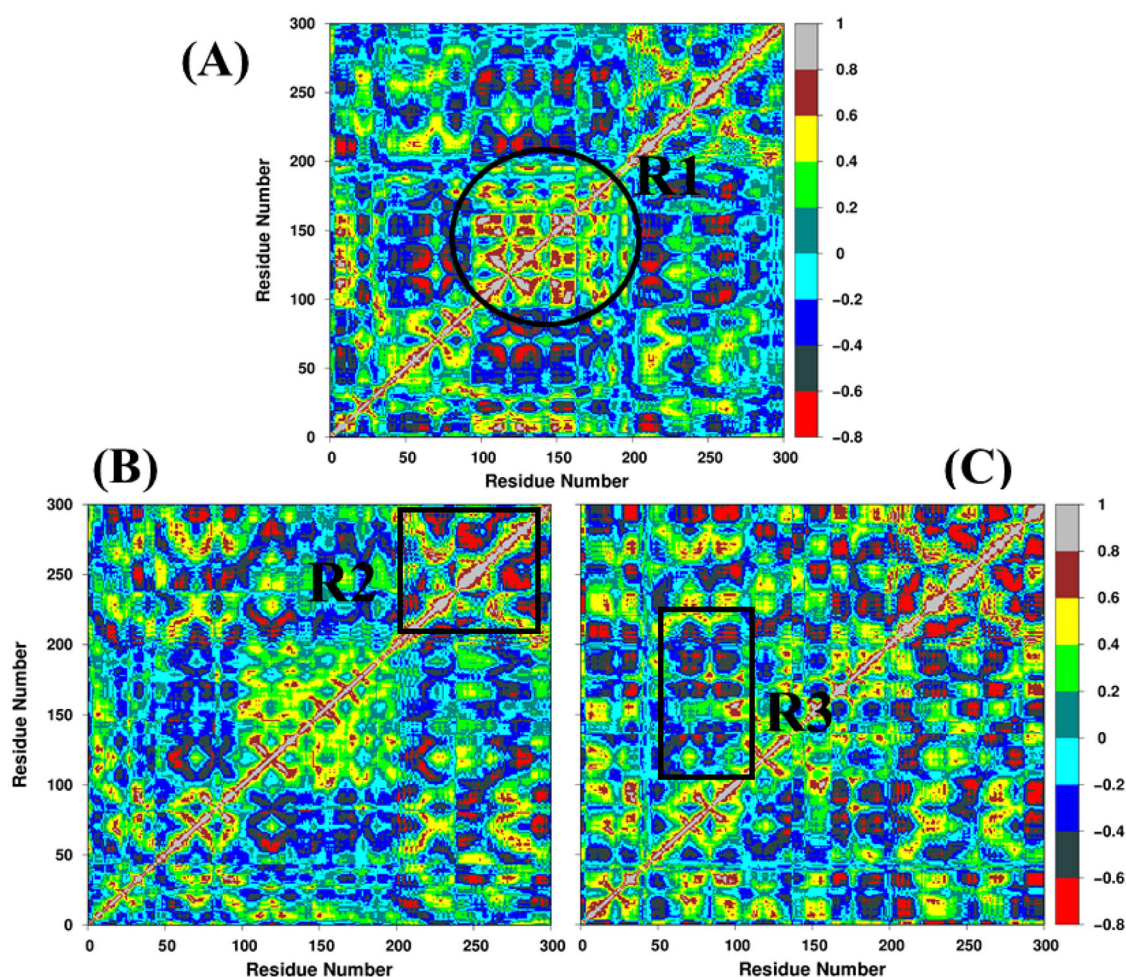


Figure 4. Dynamic cross-correlation map (DCCM) for (A) apo, (B) 3CL^{PRO}/α-ketoamide, and (C) 3CL^{PRO}/Z31792168. The extent of correlated and anti-correlated motions are color-coded. Red color shows more anti-correlated motions, and grey color shows correlated motions.

slight increase in the apparent anti-correlated motions is observed for both complexes.

In the case of the apo system, domain I (residues 8-101) displays correlated motions while domain II (or R1 in Figure 4(A)) (residues 102-184) shows highly anti-correlated movements. However, domain III (residues 201-306) has a lower strength of anti-correlation motions relative to domain I. In the case of 3CL^{PRO}/α-ketoamide (Figure 4(B)), the region R1, which represents the binding cavity, displays a significant reduction in anti-correlated and an increase in correlated motions compared to apo. In contrast to 3CL^{PRO}/α-ketoamide, more anti-correlated motions are observed in R1 for 3CL^{PRO}/Z31792168 (Figure 4(C)). Further, it is evident from Figure 4(A–C) that the inhibitor binding increases the strength of anti-correlated motions in the region R2, which indicates the residual motion of domain III. In region R3, the anti-correlated movements are diminished in 3CL^{PRO}/α-ketoamide compared to 3CL^{PRO}/Z31792168. Overall, the binding of α-ketoamide with 3CL^{PRO} creates a stable environment near the binding cavity.

3.3. Principal component analysis

To further characterize the effect of inhibitor binding on the dynamics of 3CL^{PRO} and extract the structural variations in detail, PCA was applied to the coordinates of the backbone

atoms of all three systems. The PCA results in terms of eigenvectors ($3N$, $3 \times 306 = 918$) versus eigenvalues obtained by diagonalization of the atomic fluctuations covariance matrix for complexes and apo 3CL^{PRO} are shown in Figure S2 (Supporting Information). The collective motions of the localized fluctuations can be defined by the first few principal components. The first 10 eigenvectors capture \square 87%, \square 88%, and \square 89% of the total motion in apo, 3CL^{PRO}/α-ketoamide, and 3CL^{PRO}/Z31792168.

In general, the two largest principal components (PC1 and PC2) account for more than 70% of the overall fluctuations for apo and the inhibitor-bound 3CL^{PRO}. The two-dimensional free energy landscapes (FELs) of all three systems are shown in Figure 5(A–C). It is notable that the conformational space sampled in the case of 3CL^{PRO}/α-ketoamide is more restricted, whereas a wider conformational space is sampled in cases of apo and 3CL^{PRO}/Z31792168 (see Figure 5 and Figure S3). This observation suggests that both apo and 3CL^{PRO}/Z31792168 systems are more flexible compared to 3CL^{PRO}/α-ketoamide, which agrees with the RMSF plot (Figure 3). FELs of apo (Figure 5(A)) and 3CL^{PRO}/Z31792168 (Figure 5(C)) are characterized by two dispersed free energy basins, whereas, in the case of 3CL^{PRO}/α-ketoamide (Figure 5(B)), we have obtained a single and stable global free energy minimum confined within a basin on the FEL. Porcupine plots are shown in

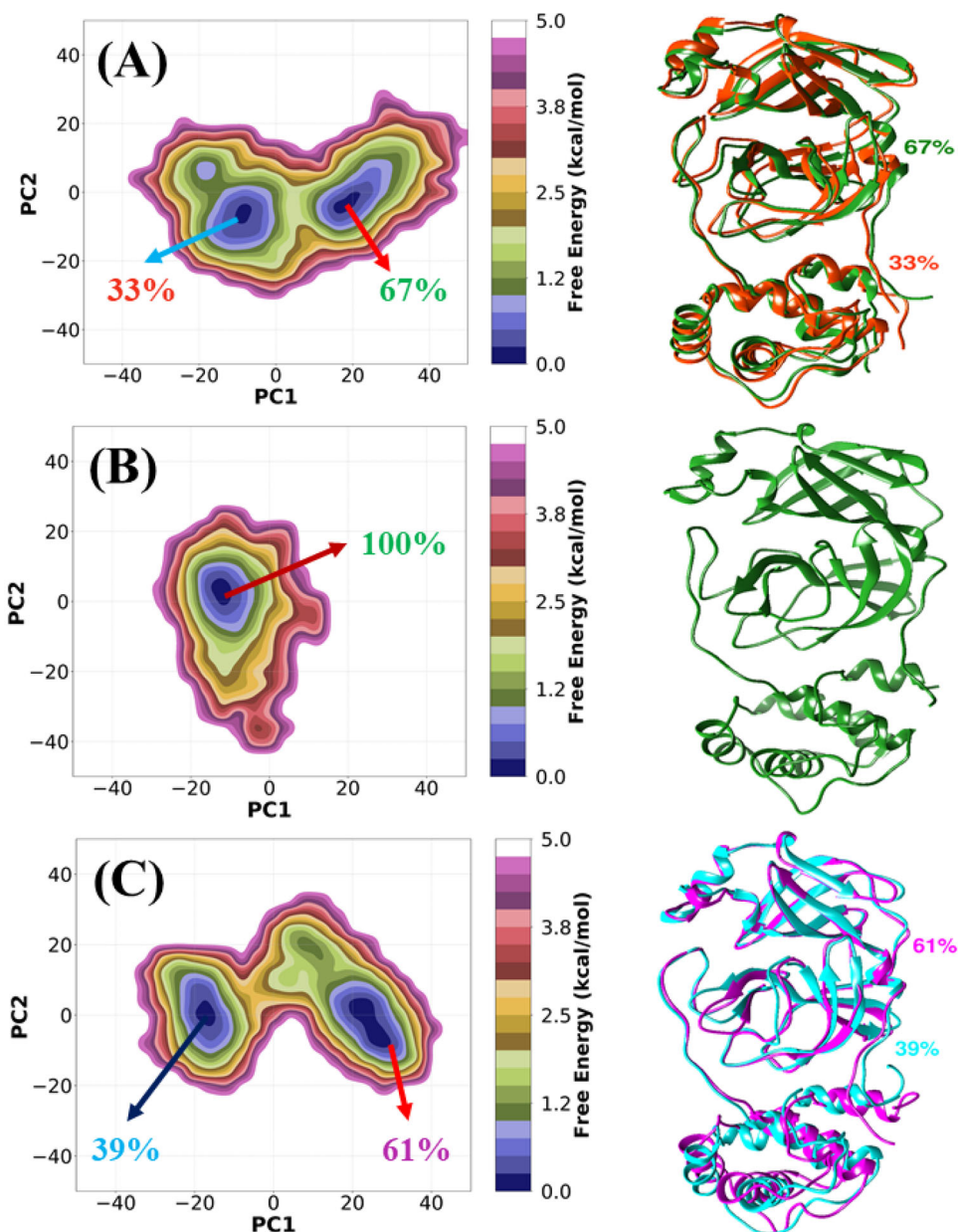


Figure 5. Two-dimensional free energy landscapes (FELs) generated by projecting the principal components, PC1 and PC2 for (A) apo, (B) 3CL^{PRO}/α-ketoamide, and (C) 3CL^{PRO}/Z31792168. The representative structures are shown on the right panel.

Supporting Information Figure S4, which was generated via the first mode that shows the largest collective motions of C_α atoms, which has been mapped onto the average structure using the Normal Modes Analysis plugin available in VMD (Humphrey et al., 1996). To visualize the detailed movements of each protein, corresponding structures were selected based on K-means (Hartigan & Wong, 1979) clusters of PCA distributions. The structures were obtained from cluster centers and superimposed with each other. Overall, it is observed that the mobility is higher for apo and 3CL^{PRO}/Z31792168 compared to the 3CL^{PRO}/α-ketoamide complex.

3.4. Dihedral principal component (dPCA) analysis of loop

Cartesian coordinates based PCA does not provide the fully correct internal and overall dynamics. However, dPCA gives us

information about internal and overall conformational dynamics. To further discover the conformational alterations of the loop (residues 185-200) connecting domains II and III, dihedral PCA (dPCA) was performed based on the dihedral angles (φ_i , ψ_i) of the peptide group in the loop (see Figure 6). The representative structures are obtained from the K-means clustering analysis and shown in Figure 6. Overall, Figure 6 indicates diverse loop conformations for each system.

The apo 3CL^{PRO} (Figure 6(A)) has one global minimum (70%) and one local minimum (30%). Similarly, the 3CL^{PRO}/α-ketoamide complex (Figure 6(B)) is characterized by two almost equiprobable free energy basins (51% and 49%). The conformational space of 3CL^{PRO}/Z31792168 is quite wider, as is evident from Figure 6(C). It is characterized by a global free energy basin (46%) and two local free energy minima (41% and 13%). In this analysis, we confirmed that this loop plays an important role in the inhibitor binding as well as

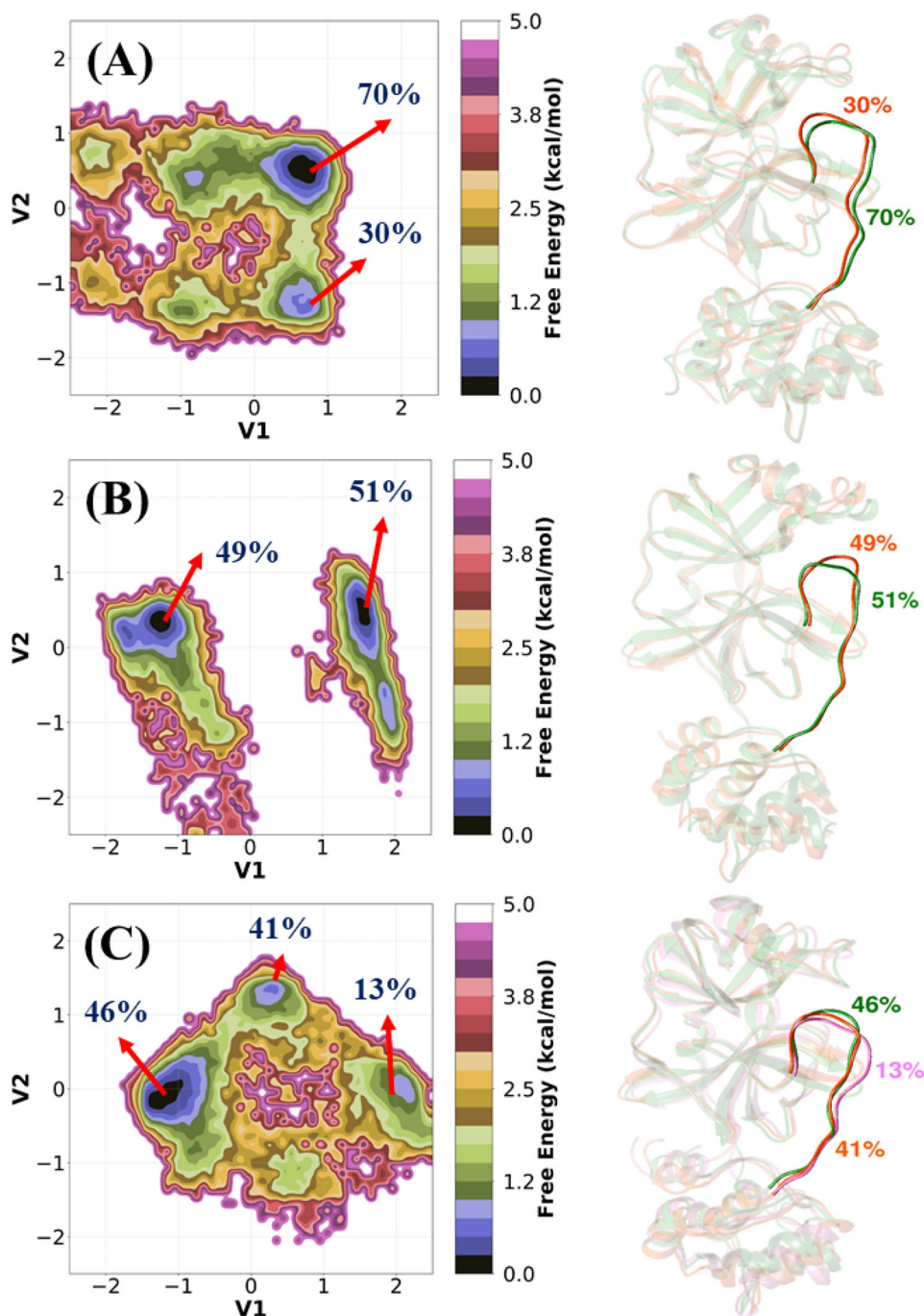


Figure 6. The two-dimensional free energy landscapes (FELs) of (A) apo, (B) 3CL^{PRO}/α-ketoamide, and (C) 3CL^{PRO}/Z31792168. FEL obtained from dPCA and their representative structures are shown on the right-hand panel.

controls the dynamical nature of 3CL^{PRO}. Finally, the inhibitor-induced fluctuation of this loop in 3CL^{PRO} demands more attention to the design of next-generation drugs.

3.5. Binding free energy analysis

To understand the biophysical basis of the molecular recognition of inhibitors by the receptor (3CL^{PRO}), the MD/MM-PBSA scheme was employed. It provides different individual components, such as ΔE_{vdW} , ΔE_{elec} , ΔG_{polr} , ΔG_{np} , and $T\Delta S$, to the total binding free energy (ΔG_{Bind}^{sim}). For binding free energy calculations of both

complexes, 2000 structures were taken from the stable region, and 50 structures were considered for the entropy calculations.

A summary of binding components in the binding free energy of inhibitors with 3CL^{PRO} is shown graphically in Figure 7, and the data are listed in Table 2. It is evident from Table 2 that the intermolecular van der Waals (ΔE_{vdW}), electrostatic interactions (ΔE_{elec}) and non-polar solvation energy (ΔG_{np}) favored the binding, while polar solvation free energy (ΔG_{pol}) and the configurational entropy ($-T\Delta S$) disfavoured the complexation. For both cases, the net polar contribution ($\Delta E_{elec} + \Delta G_{pol}$) is positive, which means that the van der Waals interactions mainly drive the binding.

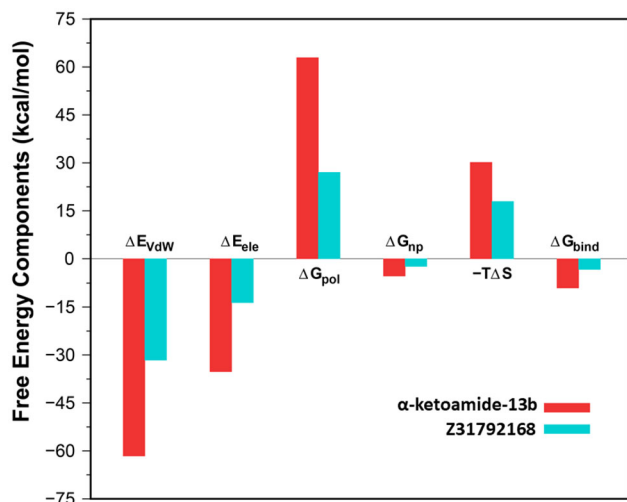


Figure 7. Energy components (kcal/mol) for the binding of inhibitors to the 3CL^{PRO}. ΔE_{vdW}, van der Waals energy; ΔE_{elec}, electrostatics energy in the gas phase; ΔG_{polar}, polar solvation energy; ΔG_{nonpolar}, nonpolar solvation energy; TΔS_{MM}, configurational entropy contribution and ΔG_{bind}, total binding energy.

Further, Table 2 reveals that the estimated binding free energy (ΔG_{Bind}^{sim}) of α-ketoamide is higher (-9.05 kcal/mol) than Z31792168 (-3.25 kcal/mol) although in the case of 3CL^{PRO}/α-ketoamide, unfavourable contributions from both ΔG_{pol} (62.94 kcal/mol) and -TΔS (30.18 kcal/mol) are relatively higher compared to 3CL^{PRO}/Z31792168 (ΔG_{pol} = 27.08 kcal/mol, TΔS = 17.92 kcal/mol). This is because ΔE_{vdW} and ΔE_{elec} are more favorable in 3CL^{PRO}/α-ketoamide (ΔE_{vdW} = -61.63 kcal/mol, ΔE_{elec} = -35.23 kcal/mol) than 3CL^{PRO}/Z31792168 (ΔE_{vdW} = -31.61 kcal/mol, ΔE_{elec} = -13.64 kcal/mol). Overall, our study suggests that α-ketoamide is more potent against COVID-19 main protease compared to Z31792168.

Next, in our study, the binding affinity of α-ketoamide was further evaluated and compared with the FDA approved anti-HIV protease inhibitors, such as lopinavir and darunavir, which has been reported as potent drugs against 3CL^{PRO} of SARS-CoV-2. Recently, the molecular recognition of lopinavir by the COVID-19 3CL^{PRO} has been investigated using the MMPBSA scheme (Wang, 2020), and the binding free energy of lopinavir was found to be lesser (-6.63 kcal/mol) than α-ketoamide (-9.05 kcal/mol) (see Table 2). It is further revealed that the electrostatic interaction (-52.46 kcal/mol) favored the complex formation more compared to the van der Waals interactions (-20.09 kcal/mol). This is in contrast to what has been observed for α-ketoamide. In the case of α-ketoamide, the van der Waals interactions energy is more favorable compared to the intermolecular electrostatic interactions. Similarly, in the case of darunavir/3CL^{PRO}, the van der Waals force is more favorable (-41.32 kcal/mol) than the electrostatic force (-5.80 kcal/mol) (Sang et al., 2020). Our study reports that the binding affinity decreases in the following order against COVID-19 3CL^{PRO}: α-ketoamide > lopinavir > darunavir > Z31792168 (See Table 2). Therefore, the inhibitor, α-ketoamide may be considered as a lead compound in the discovery of rational drugs against COVID-19.

Subsequently, we explored the critical residues involved in the receptor-ligand binding by performing the per-residue decomposition of free energy using MMGBSA. The receptor-ligand interaction spectra were shown in Figure 8. A hotspot

Table 2. Energetic components of the binding free energy for SARS-CoV-2-inhibitors complexes calculated using MM-PBSA (kcal/mol). Standard errors of the mean (SEM) are provided in parentheses.

Components	α-ketoamide	Z31792168	Lopinavir (Wang, 2020)	Darunavir (Sang et al., 2020)
ΔE _{vdW}	-61.63 (0.10)	-31.61 (0.06)	-20.09 (0.63)	-41.32
ΔE _{elec}	-35.23 (0.13)	-13.64 (0.09)	-52.46 (0.33)	-5.80
ΔG _{pol}	62.94 (0.13)	27.08 (0.09)	46.58 (0.56)	29.01
ΔG _{np}	-5.31 (0.00)	-2.99 (0.00)	-4.59 (0.02)	-4.75
ΔG _{solv} ^a	57.63 (0.13)	24.09 (0.09)	41.99 (0.56)	24.26
ΔG _{pol} + elec ^b	27.71 (0.18)	13.44 (0.13)	-5.88 (0.65)	23.21
ΔE _{MM} ^c	-96.86 (0.16)	-45.25 (0.11)	-30.56 (0.71)	-47.12
TΔS ^d	30.18 (0.81)	17.92 (0.88)	-23.93 (0.01)	NA
ΔG _{Total} ^e	-39.23 (0.11)	-21.16 (0.01)	-30.56	-22.86
ΔG _{bind} ^{sim}	-9.05 (0.82)	-3.25 (0.88)	-6.63 (0.28)	NA
IC ₅₀ ^{Exp}	0.67 ± 0.18 μM	NA	NA	NA

$$^a \Delta G_{solv} = \Delta G_{np} + \Delta G_{pol};$$

$$^b \Delta G_{pol} + elec = \Delta E_{elec} + \Delta G_{pol};$$

$$^c \Delta E_{MM} = \Delta E_{vdW} + \Delta E_{elec};$$

$$^d \Delta S = \text{configuration entropy};$$

$$^e \Delta G = E_{vdW} + \Delta E_{elec} + \Delta G_{np} + \Delta G_{pol}, \Delta G_{Bind}^{sim} = E_{vdW} + \Delta E_{elec} + \Delta G_{np} + \Delta G_{pol} - (T\Delta S).$$

residue is considered in the MM-GBSA interaction energy when it is higher than -1.0 kcal/mol and reported in Table 3. It is evident from Table 2 that a more significant number of hotspot residues (Met165, Leu27, His164, His41, Glu166, Cys145, Pro168, and His163) contributes favorably to the binding of α-ketoamide in comparison to Z31792168 (Met165, His163, and His164). This might be one of the reasons for the higher affinity of α-ketoamide relative to Z31792168 against 3CL^{PRO}. It can further be observed from Table 3 that the catalytic dyad, His41 (-2.32 kcal/mol), and Cys145 (-1.32 kcal/mol) contribute more significantly to the binding of α-ketoamide than Z31792168. Overall, the identification of hotspot residues from our analysis can facilitate the discovery of new selective inhibitor against COVID-19 3CL^{PRO}.

Subsequently, to compliment the above results, we have performed the hydrogen bond (H-bond) analysis for both the complexes on their respective MD trajectories and the H-bond occupancies are reported in Table 4. It is observed from Table 4 that in the case of 3CL^{PRO}/α-ketoamide, residues His41, Glu166, and His164 (~ 42%) form H-bond with the inhibitor with an occupancy of > 40% during the simulation. However, in the case of 3CL^{PRO}/Z31792168, the highest H-bond occupancy is obtained for only Glu166 (~ 35%). This explains why the intermolecular electrostatic interaction is stronger in 3CL^{PRO}/α-ketoamide compared to 3CL^{PRO}/Z31792168. Besides, the number of H-bond as a function of simulations time is shown in Figure S5 (Supporting Information), which also ensures that a higher number of H-bond persists for 3CL^{PRO}/α-ketoamide compared to 3CL^{PRO}/Z31792168, suggesting the strong bonding of the inhibitor α-ketoamide with 3CL^{PRO}.

A detailed interaction profile of residues involving H-bond and hydrophobic interactions is also computed using LigPlot (Wallace et al., 1995) and shown in Figure 9. It suggests that one of the catalytic dyad residues, His41 plays a significant role in forming a strong H-bond with α-ketoamide. Also, the hydrophobic contacts resulting from the hydrophobic residues for both the complexes throughout the simulations were computed and shown in Supporting Information Figure S6. It also suggests the highest number of hydrophobic

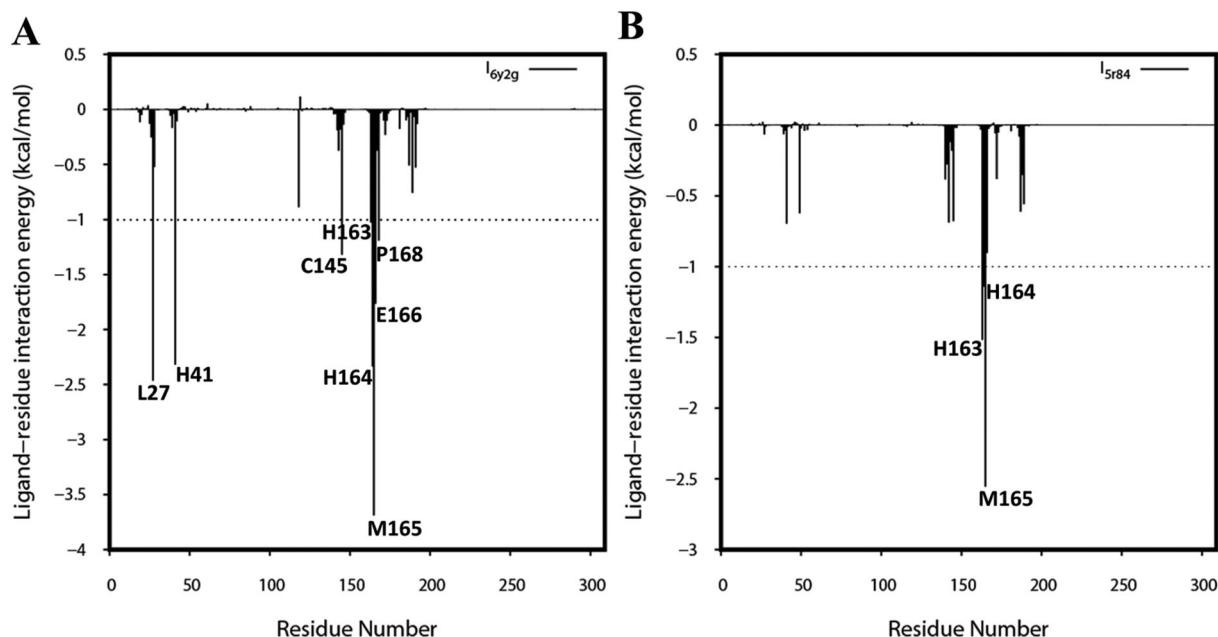


Figure 8. Decomposition of $\Delta G_{\text{bind}}^{\text{sim}}$ into contributions from individual residues for (A) 3CL^{PRO}/ α -ketoamide and (B) 3CL^{PRO}/Z31792168.

Table 3. Decomposition of binding free energy into contributions from individual residues^a.

Residue	E_{vdW}	E_{elec}	G_{pol}	G_{np}	$G_{\text{side_chain}}$	G_{backbone}	G_{total}
3CL ^{PRO} / α -ketoamide							
Met165	-2.95	-1.82	1.30	-0.23	-2.03	-1.67	-3.70
Leu27	-2.05	-0.47	0.23	-0.18	-1.79	-0.68	-2.47
His164	-1.80	-4.15	3.70	-0.09	-0.31	-2.03	-2.34
His41	-2.04	-2.49	2.43	-0.22	-2.18	-0.14	-2.32
Glu166	-3.10	-4.14	5.99	-0.51	-0.37	-1.39	-1.76
Cys145	-1.86	-0.56	1.26	-0.16	-1.08	-0.24	-1.32
Pro168	-1.07	-0.02	0.13	-0.23	-0.79	-0.40	-1.19
His163	-0.54	-2.98	2.56	-0.06	-0.96	-0.06	-1.02
3CL ^{PRO} /Z31792168							
Met165	-2.11	-1.07	0.82	-0.20	-1.47	-1.09	-2.56
His163	-0.37	-2.86	1.74	-0.03	-1.43	-0.09	-1.52
His164	-0.95	-2.24	2.12	-0.08	-0.23	-0.92	-1.15

^aEnergetic contributions from the van der Waals (E_{vdW}) and electrostatic interactions (E_{elec}) as well as polar (G_{pol}) and nonpolar solvation energy (G_{np}) and the total contribution of given residue (G_{total}) for SARS-CoV-2-inhibitor complexes are listed. $G_{\text{side_chain}}$ and G_{backbone} represent the side chain and backbone contributions. Only residues with $|\Delta G| \geq 1.0$ kcal/mol are shown. All values are given in kcal/mol.

Table 4. The hydrogen bonds formed between SARS-CoV-2 and inhibitor and the corresponding average distance and percent determined using the MD trajectories in the MD simulations.

Binding couples		MD	
Acceptor	Donor	Avg. Distance (\AA) ^a	Occupancy (%) ^b
3CL ^{PRO} / α -ketoamide			
Lig@O40	His41@NE2	2.88	43.12
Lig@O22	Glu166@N	2.90	42.53
His164@O	Lig@N38	2.88	41.76
Lig@O48	His163@NE2	2.83	29.97
Glu166@O	Lig@N23	2.87	24.43
Glu166@OE2	Lig@N49	2.84	23.06
Glu166@OE1	Lig@N49	2.84	13.17
Leu27@HD23	Lig@N36	2.82	10.33
Leu27@HD21	Lig@N36	2.83	10.25
Leu27@HD22	Lig@N36	2.84	09.78
Asn142@OD1	Lig@N36	2.82	09.56
Lig@O41	Gly143@N	2.84	07.98
Lig@H20	Gln189@N	2.85	05.10
3CL ^{PRO} /Z31792168			
Lig@O	Glu166@N	2.87	34.55
His164@O	Lig@N	2.84	25.34
Lig@N1	His163@NE2	2.91	09.19

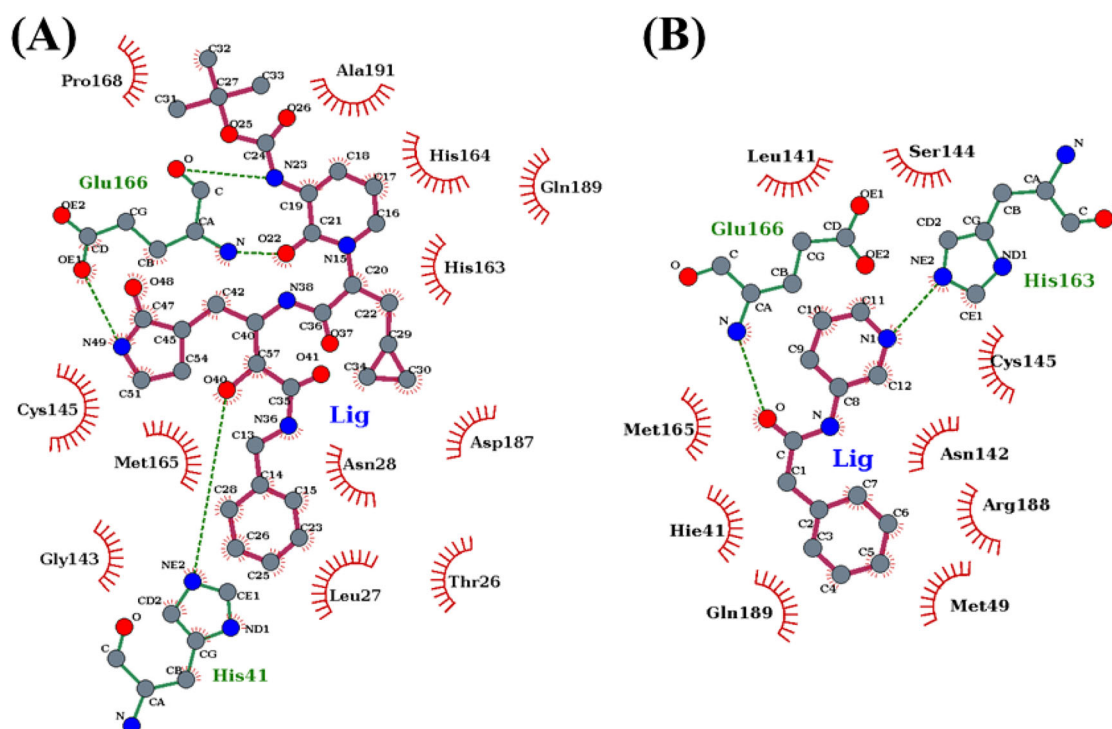


Figure 9. The receptor-ligand interaction profile for (A) α -ketoamide and (B) Z31792168. The plots are generated by using Ligplot+. Hydrogen bonds are shown as green dotted lines. Red semicircles show the residues involved in the hydrophobic contacts, and residues involved in hydrogen bonds are represented in green. The inhibitors are described as balls and sticks.

contacts remain in the case of 3CL^{PRO}/ α -ketoamide, which is in agreement with the finding that the net nonpolar interaction ($\Delta E_{vdW} + \Delta G_{np}$) is more favorable in 3CL^{PRO}/ α -ketoamide compared to 3CL^{PRO}/Z31792168. Overall, our investigations reveal that α -ketoamide is a more potent lead molecule against 2019-nCoV 3CL^{PRO} than the FDA approved anti-HIV1 protease inhibitors, such as lopinavir and darunavir which is being recently focused in the treatment of COVID-19.

4. Conclusion

The recent outbreak of COVID-19 has caused a severe strain in the public health system in many countries. COVID-19 can cause mild to severe illness. The current situation demands an efficacious vaccine or novel antiviral drugs targeting COVID-19. Herein, we have studied the mechanism of binding of two potential inhibitors, namely α -ketoamide and Z31792168 to COVID-19 main protease (3CL^{PRO}) by using an atomistic molecular dynamics simulation of 100 ns in conjunction with the widely used molecular mechanics/Poisson-Boltzmann surface area (MM/PBSA) scheme. Our study shows that the 3CL^{PRO}-inhibitor complexation is favored by the intermolecular van der Waals and electrostatic interactions as well as nonpolar solvation free energy. We have also demonstrated that the inhibitor α -ketoamide is more potent compared to Z31792168 due to an increased favorable contribution from the intermolecular van der Waals and electrostatic interactions relative to Z31792168. Furthermore, in the case of α -ketoamide, the nonpolar component of the solvation free energy is also slightly more favorable compared to Z31792168. We have also identified the hotspot residues controlling the receptor-ligand binding. Finally, our

study also reveals that α -ketoamide has a better binding affinity compared to anti-HIV retroviral drugs, such as darunavir and lopinavir. Overall, α -ketoamide can be used as a lead compound in the development of drugs targeting SARS-CoV-2 3CL^{PRO}, and our study might play a useful role for the same.

Disclosure statement

No potential conflict of interest was reported by the authors.

Funding

This work was partially supported by the Department of Biotechnology, Govt. of India (grant number BT/RLF/Re-entry/40/2014, DBT-Ramalingaswami Re-entry Fellowship), and Department of Science and Technology (DST), Govt. of India (grant number ECR/2017/000010). MFS would like to thank DST, Govt. of India, for providing with the INSPIRE Fellowship (DST/INSPIRE Fellowship/2017/IF170145).

ORCID

Md Fulbabu Sk <http://orcid.org/0000-0003-4341-8370>
 Rajarshi Roy <http://orcid.org/0000-0002-5788-9424>
 Parimal Kar <http://orcid.org/0000-0001-8451-9739>

References

- Aanouz, I., Belhassan, A., El Khatabi, K., Lakhlifi, T., El Idrissi, M., & Bouachrine, M. (2020). Moroccan Medicinal plants as inhibitors of COVID-19: Computational investigations. *Journal of Biomolecular Structure and Dynamics*. <https://doi.org/10.1080/07391102.07392020.01758790>

- Abdelli, I., Hassani, F., Bekkel Brikci S., & Ghalem, S. (2020). *In silico* study the inhibition of Angiotensin converting enzyme 2 receptor of COVID-19 by *Ammoides verticillata* components harvested from western Algeria. *Journal of Biomolecular Structure and Dynamics*. <https://doi.org/10.1080/07391102.07392020.01763199>
- Alamri, M. A., ul Qamar, M. T., & Alqahtani, S. M. (2020). Pharmacoinformatics and molecular dynamic simulation studies reveal potential inhibitors of SARS-CoV-2 main protease 3CLpro. *Preprints*. <https://doi.org/10.20944/preprints202002.200308.v202001>.
- Berendsen, H. J., Postma, J. v., van Gunsteren, W. F., DiNola, A., & Haak, J. (1984). Molecular dynamics with coupling to an external bath. *The Journal of Chemical Physics*, 81(8), 3684–3690. <https://doi.org/10.1063/1.448118>
- Berman, H. M., Battistuz, T., Bhat, T. N., Bluhm, W. F., Bourne, P. E., Burkhardt, K., Feng, Z., Gilliland, G. L., Iype, L., Jain, S., Fagan, P., Marvin, J., Padilla, D., Ravichandran, V., Schneider, B., Thanki, N., Weissig, H., Westbrook, J. D., & Zardecki, C. (2002). The protein data bank. *Acta Crystallographica. Section D, Biological Crystallography*, 58(Pt 6 No 1), 899–907. <https://doi.org/10.1107/s0907444902003451>
- Boopathi, S., Poma, A. B., & Kolandaivel, P. (2020). Novel 2019 Coronavirus Structure, Mechanism of Action, Antiviral drug promises and rule out against its treatment. *Journal of Biomolecular Structure and Dynamics*. <https://doi.org/10.1080/07391102.07392020.01758788>
- Case, D. A., Ben-Shalom, I. Y., Brozell, S. R., Cerutti, D. S., Cheatham, T. E., III, Cruzeiro, V. W. D., Darden, T. A., Duke, R. E., Ghoreishi, D., Gilson, M. K., Gohlke, H., Goetz, A. W., Greene, D., Harris, R., Homeyer, N., Izadi, S., Kovalenko, A., Kurtzman, T., Lee, T. S., ... Kollman, P. A. (2018). *AMBER 2018*. University of California.
- Chang, C.-K., Hou, M.-H., Chang, C.-F., Hsiao, C.-D., & Huang, T.-H. (2014). The SARS coronavirus nucleocapsid protein-forms and functions. *Antiviral Research*, 103, 39–50. <https://doi.org/10.1016/j.antiviral.2013.12.009>
- Darden, T., York, D., & Pedersen, L. (1993). Particle mesh Ewald: An N-log (N) method for Ewald sums in large systems. *Journal of Chemical Physics*, 98(12), 10089–10092. <https://doi.org/10.1063/1.464397>
- Das, S., Sarmah, S., Lyndem, S., & Singha Roy, A. (2020). An investigation into the identification of potential inhibitors of SARS-CoV-2 main protease using molecular docking study. *Journal of Biomolecular Structure and Dynamics*. <https://doi.org/10.1080/07391102.07392020.01763201>
- Elfiky, A. A. (2020). Natural products may interfere with SARS-CoV-2 attachment to the host cell. *Journal of Biomolecular Structure and Dynamics*. <https://doi.org/10.1080/07391102.07392020.01761881>
- Elfiky, A. A. (2020). SARS-CoV-2 RNA dependent RNA polymerase (RdRp) targeting: An in silico perspective. *Journal of Biomolecular Structure and Dynamics*. <https://doi.org/10.1080/07391102.07392020.01761882>
- Elfiky, A. A., & Azzam, E. B. (2020). Novel Guanosine Derivatives against MERS CoV polymerase: An in silico perspective. *Journal of Biomolecular Structure and Dynamics*. <https://doi.org/10.1080/07391102.07392020.01758789>
- Elmezzayen, A. D., Al-Obaidi, A., Şahin, A. T., & Yelekcı, K. (2020). Drug repurposing for coronavirus (COVID-19): In silico screening of known drugs against coronavirus 3CL hydrolase and protease enzymes. *Journal of Biomolecular Structure and Dynamics*. <https://doi.org/10.1080/07391102.07392020.01758791>
- Enayatkhani, M., Hasaniyazad, M., Faezi, S., Guklani, H., Davoodian, P., Ahmadi, N., Einakian, M. A., Karmostaji, A., & Ahmadi, K. (2020). Reverse vaccinology approach to design a novel multi-epitope vaccine candidate against COVID-19: An in silico study. *Journal of Biomolecular Structure and Dynamics*. <https://doi.org/10.1080/07391102.07392020.01756411>
- Fearon, D., Powell, A. J., Douangamath, A., Owen, C. D., Wild, C., Krojer, T., Lukacik, P., Strain-Damerell, C. M., Walsh, M. A., von Delft, F. (2020). *PanDDA analysis of COVID-19 main protease against the DSI-poised Fragment Library*. <http://www.rcsb.org/structure/5R84>.
- Fiser, A., & Šali, A. (2003). Modeller: Generation and refinement of homology-based protein structure models. *Methods in Enzymology*, Elsevier, 374, 461–491.
- Frauenfelder, H., Sligar, S. G., & Wolynes, P. G. (1991). The energy landscapes and motions of proteins. *Science (New York, N.Y.)*, 254(5038), 1598–1603. <https://doi.org/10.1126/science.1749933>
- Gupta, M. K., Vemula, S., Donde, R., Gouda, G., Behera, L., & Vadde, R. (2020). In-silico approaches to detect inhibitors of the human severe acute respiratory syndrome coronavirus envelope protein ion channel. *Journal of Biomolecular Structure and Dynamics*. <https://doi.org/10.1080/07391102.07392020.01751300>
- Hartigan, J. A., & Wong, M. A. (1979). Algorithm AS 136: A k-means clustering algorithm. *Journal of the Royal Statistical Society. Series C (Applied Statistics)*, 28(1), 100–108. <https://doi.org/10.2307/2346830>
- Hasan, A., Paray, B. A., Hussain, A., Qadir, F. A., Attar, F., Aziz, F. M., Sharifi, M., Derakhshankhah, H., Rasti, B., & Mehrabi, M. (2020). A review on the cleavage priming of the spike protein on coronavirus by angiotensin-converting enzyme-2 and furin. *Journal of Biomolecular Structure and Dynamics*. <https://doi.org/10.1080/07391102.07392020.01754293>
- Hess, B., Kutzner, C., Van Der Spoel, D., & Lindahl, E. (2008). GROMACS 4: Algorithms for highly efficient, load-balanced, and scalable molecular simulation. *Journal of Chemical Theory and Computation*, 4(3), 435–447. <https://doi.org/10.1021/ct700301q>
- Hui, D. S., I Azhar, E., Madani, T. A., Ntoumi, F., Kock, R., Dar, O., Ippolito, G., Mchugh, T. D., Memish, Z. A., Drosten, C., Zumla, A., & Petersen, E. (2020). The continuing 2019-nCoV epidemic threat of novel coronaviruses to global health—The latest 2019 novel coronavirus outbreak in Wuhan. *International Journal of Infectious Diseases: IJID : Official Publication of the International Society for Infectious Diseases*, 91, 264–266. <https://doi.org/10.1016/j.ijid.2020.01.009>
- Humphrey, W., Dalke, A., & Schulten, K. (1996). VMD: Visual molecular dynamics. *Journal of Molecular Graphics*, 14(1), 33–38. [https://doi.org/10.1016/0263-7855\(96\)00018-5](https://doi.org/10.1016/0263-7855(96)00018-5)
- Hünenberger, P., Mark, A., & Van Gunsteren, W. (1995). Fluctuation and cross-correlation analysis of protein motions observed in nanosecond molecular dynamics simulations. *Journal of Molecular Biology*, 252(4), 492–503. <https://doi.org/10.1006/jmbi.1995.0514>
- Ichiye, T., & Karplus, M. (1991). Collective motions in proteins: A covariance analysis of atomic fluctuations in molecular dynamics and normal mode simulations. *Proteins: Structure, Function, and Genetics*, 11(3), 205–217. <https://doi.org/10.1002/prot.340110305>
- Islam, R., Parves, R., Paul, A. S., Uddin, N., Rahman, M. S., Mamun, A. A., Hossain, M. N., Ali, M. A., & Halim, M. A. (2020). A Molecular Modeling Approach to Identify Effective Antiviral Phytochemicals against the Main Protease of SARS-CoV-2. *Journal of Biomolecular Structure and Dynamics*. <https://doi.org/10.1080/07391102.07392020.01761883>
- Jakalian, A., Jack, D. B., & Bayly, C. I. (2002). Fast, efficient generation of high-quality atomic charges. AM1-BCC model: II. Parameterization and validation. *Journal of Computational Chemistry*, 23(16), 1623–1641. <https://doi.org/10.1002/jcc.10128>
- Jin, Z., Du, X., Xu, Y., Deng, Y., Liu, M., Zhao, Y., Zhang, B., Li, X., Zhang, L., & Peng, C. (2020). Structure of Mpro from COVID-19 virus and discovery of its inhibitors. *Nature*. <https://doi.org/10.1038/s41586-41020-42223-y>.
- Jonniya, N. A., & Kar, P. (2020). Investigating specificity of the anti-hypertensive inhibitor WNK463 against With-No-Lysine kinase family isoforms via multiscale simulations. *Journal of Biomolecular Structure & Dynamics*, 38(5), 1306–1321. <https://doi.org/10.1080/07391102.2019.1602079>
- Jonniya, N. A., SK, M. F., & Kar, P. (2019). Investigating Phosphorylation-Induced Conformational Changes in WNK1 Kinase by Molecular Dynamics Simulations. *ACS Omega*, 4(17), 17404–17416. <https://doi.org/10.1021/acsomega.9b02187>
- Joshi, R. S., Jagdale, S. S., Bansode, S. B., Shankar, S. S., Tellis, M. B., Pandya, V. K., Chugh, A., Giri, A. P., & Kulkarni, M. J. (2020). Discovery of potential multi-target-directed ligands by targeting host-specific SARS-CoV-2 structurally conserved main protease. *Journal of Biomolecular Structure and Dynamics*. <https://doi.org/10.1080/07391102.07392020.01760137>
- Kar, P., & Knecht, V. (2012a). Energetic basis for drug resistance of HIV-1 protease mutants against amprenavir. *Journal of Computer-Aided Molecular Design*, 26(2), 215–232. <https://doi.org/10.1007/s10822-012-9550-5>
- Kar, P., & Knecht, V. (2012b). Energetics of mutation-induced changes in potency of lersivirine against HIV-1 reverse transcriptase. *The Journal*

- of *Physical Chemistry B*, 116(22), 6269–6278. <https://doi.org/10.1021/jp300818c>
- Kar, P., & Knecht, V. (2012c). Mutation-induced loop opening and energetics for binding of tamiflu to influenza N8 neuraminidase. *The Journal of Physical Chemistry B*, 116(21), 6137–6149. <https://doi.org/10.1021/jp3022612>
- Kar, P., & Knecht, V. (2012d). Origin of decrease in potency of darunavir and two related antiviral inhibitors against HIV-2 compared to HIV-1 protease. *The Journal of Physical Chemistry B*, 116(8), 2605–2614. <https://doi.org/10.1021/jp211768n>
- Kar, P., Lipowsky, R., & Knecht, V. (2011). Importance of polar solvation for cross-reactivity of antibody and its variants with steroids. *The Journal of Physical Chemistry B*, 115(23), 7661–7669. <https://doi.org/10.1021/jp201538t>
- Kar, P., Lipowsky, R., & Knecht, V. (2013). Importance of polar solvation and configurational entropy for design of antiretroviral drugs targeting HIV-1 protease. *The Journal of Physical Chemistry B*, 117(19), 5793–5805. <https://doi.org/10.1021/jp3085292>
- Kar, P., Seel, M., Hansmann, U. H., & Höfinger, S. (2007). Dispersion Terms and Analysis of size- and charge dependence in an enhanced Poisson-Boltzmann approach. *The Journal of Physical Chemistry B*, 111(30), 8910–8918. <https://doi.org/10.1021/jp072302u>
- Kar, P., Wei, Y., Hansmann, U. H., & Höfinger, S. (2007). Systematic study of the boundary composition in Poisson Boltzmann calculations. *Journal of Computational Chemistry*, 28(16), 2538–2544. <https://doi.org/10.1002/jcc.20698>
- Khan, R. J., Jha, R. K., Amera, G., Jain, M., Singh, E., Pathak, A., Singh, R. P., Muthukumar, J., & Singh, A. K. (2020). Targeting SARS-CoV-2: A systematic drug repurposing approach to identify promising inhibitors against 3C-like Proteinase and 2'-O-RiboseMethyltransferase. *Journal of Biomolecular Structure and Dynamics*. <https://doi.org/10.1080/07391102.07392020.01753577>
- Khan, S. A., Zia, K., Ashraf, S., Uddin, R., & Ul-Haq, Z. (2020). Identification of Chymotrypsin-like Protease Inhibitors of SARS-CoV-2 Via Integrated Computational Approach. *Journal of Biomolecular Structure and Dynamics*. <https://doi.org/10.1080/07391102.07392020.01751298>
- Kollman, P. A., Massova, I., Reyes, C., Kuhn, B., Huo, S., Chong, L., Lee, M., Lee, T., Duan, Y., Wang, W., Donini, O., Cieplak, P., Srinivasan, J., Case, D. A., & Cheatham, T. E. (2000). Calculating structures and free energies of complex molecules: Combining molecular mechanics and continuum models. *Accounts of Chemical Research*, 33(12), 889–897. <https://doi.org/10.1021/ar000033j>
- Kräutler, V., van Gunsteren, W. F., & Hünenberger, P. H. (2001). A fast SHAKE algorithm to solve distance constraint equations for small molecules in molecular dynamics simulations. *Journal of Computational Chemistry*, 22(5), 501–508. [https://doi.org/10.1002/1096-987X\(20010415\)22:5<501::AID-JCC1021>3.0.CO;2-V](https://doi.org/10.1002/1096-987X(20010415)22:5<501::AID-JCC1021>3.0.CO;2-V)
- Lin, S., Shen, R., He, J., Li, X., & Guo, X. (2020). Molecular modeling evaluation of the binding effect of ritonavir, lopinavir and darunavir to severe acute respiratory syndrome coronavirus 2 proteases. *bioRxiv*. <https://doi.org/10.1101/2020.1101.1131.929695>
- Loncharich, R. J., Brooks, B. R., & Pastor, R. W. (1992). Langevin dynamics of peptides: The frictional dependence of isomerization rates of N-acetylalanyl-N'-methylamide. *Biopolymers: Original Research on Biomolecules*, 32(5), 523–535. <https://doi.org/10.1002/bip.360320508>
- Maier, J. A., Martinez, C., Kasavajhala, K., Wickstrom, L., Hauser, K. E., & Simmerling, C. (2015). ff14SB: improving the accuracy of protein side chain and backbone parameters from ff99SB. *Journal of Chemical Theory and Computation*, 11(8), 3696–3713. <https://doi.org/10.1021/acs.jctc.5b00255>
- McCammon, J. (1984). Protein dynamics. *Reports on Progress in Physics*, 47(1), 1–46. <https://doi.org/10.1088/0034-4885/47/1/001>
- Muralidharan, N., Sakthivel, R., Velmurugan, D., & Gromiha, M. M. (2020). Computational studies of drug repurposing and synergism of lopinavir, oseltamivir and ritonavir binding with SARS-CoV-2 Protease against COVID-19. *Journal of Biomolecular Structure and Dynamics*. <https://doi.org/10.1080/07391102.07392020.01752802>
- Olsson, M. H., Søndergaard, C. R., Rostkowski, M., & Jensen, J. H. (2011). PROPKA3: Consistent treatment of internal and surface residues in empirical pKa Predictions. *Journal of Chemical Theory and Computation*, 7(2), 525–537. <https://doi.org/10.1021/ct100578z>
- Onufriev, A., Bashford, D., & Case, D. A. (2004). Exploring protein native states and large-scale conformational changes with a modified generalized born model. *Proteins: Structure, Function, and Bioinformatics*, 55(2), 383–394. <https://doi.org/10.1002/prot.20033>
- Pant, S., Singh, M., Ravichandiran, V., Murty, U., & Srivastava, H. K. (2020). Peptide-like and small-molecule inhibitors against Covid-19. *Journal of Biomolecular Structure and Dynamics*. <https://doi.org/10.1080/07391102.07392020.01757510>
- Pettersen, E. F., Goddard, T. D., Huang, C. C., Couch, G. S., Greenblatt, D. M., Meng, E. C., & Ferrin, T. E. (2004). UCSF Chimera—a visualization system for exploratory research and analysis. *Journal of Computational Chemistry*, 25(13), 1605–1612. <https://doi.org/10.1002/jcc.20084>
- Price, D. J., & Brooks, C. L. III, (2004). A modified TIP3P water potential for simulation with Ewald summation. *The Journal of Chemical Physics*, 121(20), 10096–10103. <https://doi.org/10.1063/1.1808117>
- Roe, D. R., & Cheatham, T. E. III, (2013). PTRAJ and CPPTRAJ: Software for processing and analysis of molecular dynamics trajectory data. *Journal of Chemical Theory and Computation*, 9(7), 3084–3095. <https://doi.org/10.1021/ct400341p>
- Rota, P. A., Oberste, M. S., Monroe, S. S., Nix, W. A., Campagnoli, R., Icenogle, J. P., Peñaranda, S., Bankamp, B., Maher, K., Chen, M.-H., Tong, S., Tamin, A., Lowe, L., Frace, M., DeRisi, J. L., Chen, Q., Wang, D., Erdman, D. D., Peret, T. C. T., ... Bellini, W. J. (2003). Characterization of a novel coronavirus associated with severe acute respiratory syndrome. *Science (New York, N.Y.)*, 300(5624), 1394–1399. <https://doi.org/10.1126/science.1085952>
- Roy, R., Ghosh, B., & Kar, P. (2020). Investigating conformational dynamics of Lewis Y Oligosaccharides and elucidating blood group dependency of cholera using molecular dynamics. *ACS Omega*, 5(8), 3932–3942. <https://doi.org/10.1021/acsomega.9b03398>
- Salomon-Ferrer, R., Case, D. A., & Walker, R. C. (2013). An overview of the Amber biomolecular simulation package. *Wiley Interdisciplinary Reviews: Computational Molecular Science*, 3(2), 198–210. <https://doi.org/10.1002/wcms.1121>
- Sang, P., Tian, S.-H., Meng, Z.-H., & Yang, L.-Q. (2020). Insight derived from molecular docking and molecular dynamics simulations into the binding interactions between HIV-1 protease inhibitors and SARS-CoV-2 3CLpro. *ChemRxiv*. <https://doi.org/10.26434/chemrxiv.11932995.v11932991>
- Sarma, P., Sekhar, N., Prajapat, M., Avti, P., Kaur, H., Kumar, S., Singh, S., Kumar, H., Prakash, A., & Dhibar, D. P. (2020). In-silico homology assisted identification of inhibitor of RNA binding against 2019-nCoV N-protein (N terminal domain). *Journal of Biomolecular Structure and Dynamics*. <https://doi.org/10.1080/07391102.07392020.01753580>
- Sinha, S. K., Shakya, A., Prasad, S. K., Singh, S., Gurav, N. S., Prasad, R. S., & Gurav, S. S. (2020). An in-silico evaluation of different Saikosaponins for their potency against SARS-CoV-2 using NSP15 and fusion spike glycoprotein as targets. *Journal of Biomolecular Structure and Dynamics*. <https://doi.org/10.1080/07391102.07392020.01762741>
- Sk, M. F., Roy, R., & Kar, P. (2020). Exploring the potency of currently used drugs against HIV-1 protease of subtype D variant by using multiscale simulations. *Journal of Biomolecular Structure and Dynamics*. <https://doi.org/10.1080/07391102.07392020.01724196>
- Umesh, D. K., Selvaraj, C., Singh, S. K., & Dubey, V. K. (2020). Identification of new anti-nCoV drug chemical compounds from Indian spices exploiting SARS-CoV-2 main protease as target. *Journal of Biomolecular Structure and Dynamics*. <https://doi.org/10.1080/07391102.07392020.01763202>
- Wahedi, H. M., Ahmad, S., & Abbasi, S. W. (2020). Stilbene-based natural compounds as promising drug candidates against COVID-19. *Journal of Biomolecular Structure and Dynamics*. <https://doi.org/10.1080/07391102.07392020.01762743>
- Wallace, A. C., Laskowski, R. A., & Thornton, J. M. (1995). LIGPLOT: A program to generate schematic diagrams of protein-ligand interactions. *Protein Engineering, Design and Selection*, 8(2), 127–134. <https://doi.org/10.1093/protein/8.2.127>
- Wan, Y., Shang, J., Graham, R., Baric, R. S., & Li, F. (2020). Receptor recognition by the novel coronavirus from wuhan: An analysis based on

- decade-long structural studies of SARS coronavirus. *Journal of Virology*, 94(7), e00127–00120. <https://doi.org/10.1128/JVI.00127-20>
- Wang, J. (2020). Fast identification of possible drug treatment of coronavirus disease-19 (COVID-19) through computational drug repurposing study. *Journal of Chemical Information and Modeling*. <https://doi.org/10.1021/acs.jcim.1020c00179>
- Wang, J., Wang, W., Kollman, P. A., & Case, D. A. (2001). Antechamber: An accessory software package for molecular mechanical calculations. *J. Am. Chem. Soc.*, 222, U403.
- Wang, J., Wang, W., Kollman, P. A., & Case, D. A. (2006). Automatic atom type and bond type perception in molecular mechanical calculations. *Journal of Molecular Graphics & Modelling*, 25(2), 247–260. <https://doi.org/10.1016/j.jmgs.2005.12.005>
- Wang, J., Wolf, R. M., Caldwell, J. W., Kollman, P. A., & Case, D. A. (2004). Development and testing of a general amber force field. *Journal of Computational Chemistry*, 25(9), 1157–1174. <https://doi.org/10.1002/jcc.20035>
- Webb, B., & Sali, A. (2014). Comparative protein structure modeling using MODELLER. *Current Protocols in Bioinformatics*, 47(1), 5.6.1–5.6.32. 5.6.1–5.6.32. <https://doi.org/10.1002/0471250953.bi0506s47>
- Woo, P. C., Huang, Y., Lau, S. K., & Yuen, K.-Y. (2010). Coronavirus genomics and bioinformatics analysis. *Viruses*, 2(8), 1804–1820. <https://doi.org/10.3390/v2081803>
- Wu, J. T., Leung, K., & Leung, G. M. (2020). Nowcasting and forecasting the potential domestic and international spread of the 2019-nCoV outbreak originating in Wuhan, China: A modelling study. *The Lancet*, 395(10225), 689–697. [https://doi.org/10.1016/S0140-6736\(20\)30260-9](https://doi.org/10.1016/S0140-6736(20)30260-9)
- Xu, B., Shen, H., Zhu, X., & Li, G. (2011). Fast and accurate computation schemes for evaluating vibrational entropy of proteins. *Journal of Computational Chemistry*, 32(15), 3188–3193. <https://doi.org/10.1002/jcc.21900>
- Zhang, L., Lin, D., Sun, X., Curth, U., Drosten, C., Sauerhering, L., Becker, S., Rox, K., & Hilgenfeld, R. (2020). Crystal structure of SARS-CoV-2 main protease provides a basis for design of improved α -ketoamide inhibitors. *Science*, 368, 409–412.